nanomaterials

MDPI

Article

One-Step Hydrothermal Synthesis of Nanostructured $MgBi_2O_6/TiO_2$ Composites for Enhanced Hydrogen Production

Feng Xu [1], Chaohao Hu [1,2,*], Di Zhu [1], Dianhui Wang [1,2], Yan Zhong [1,2], Chengying Tang [1,2] and Huaiying Zhou [1,2]

[1] School of Materials Science and Engineering, Guilin University of Electronic Technology, Guilin 541004, China; xufeng118292@163.com (F.X.); heyjude456@163.com (D.Z.); devix@mails.guet.edu.cn (D.W.); yanzhong@guet.edu.cn (Y.Z.); ctang@guet.edu.cn (C.T.); zhy@guet.edu.cn (H.Z.)

[2] Guangxi Key Laboratory of Information Materials, Guilin University of Electronic Technology, Guilin 541004, China

* Correspondence: chaohao.hu@guet.edu.cn

Abstract: A highly efficient $MgBi2O_6$ (MBO)/TiO_2 heterostructured photocatalyst for the evolution of H_2 was successfully prepared using a one-step hydrothermal method. The phase structure, microstructure and optical properties of the MBO/TiO_2 composites were investigated by various experimental techniques. A series of H_2 production experiments were performed under visible light. The measured results indicated that the nanostructured MBO/TiO_2 composite, with a stoichiometric molar ratio of MBO:TiO_2 = 0.2%, displayed the best H_2 production rate of 3413 μmol h^{-1} g^{-1}. The excellent photocatalytic performance of the obtained composite material was due to the heterojunction formed between MBO and TiO_2, which reduced the charge transfer resistance and accelerated the separation efficiency of the photogenerated electron–hole pairs. The reaction mechanism was also discussed in detail.

Keywords: $MgBi_2O_6/TiO_2$; photocatalyst; heterojunction; hydrothermal method

Citation: Xu, F.; Hu, C.; Zhu, D.; Wang, D.; Zhong, Y.; Tang, C.; Zhou, H. One-Step Hydrothermal Synthesis of Nanostructured $MgBi_2O_6/TiO_2$ Composites for Enhanced Hydrogen Production. *Nanomaterials* **2022**, *12*, 1302. https://doi.org/10.3390/nano12081302

Academic Editors: Yuichi Negishi and Giuseppe Cappelletti

Received: 7 December 2021
Accepted: 28 March 2022
Published: 11 April 2022

1. Introduction

The quick development of science and technology has facilitated peoples' lives, but has also resulted in an aggravated energy shortage and environmental deterioration. The development of clean fuels is one of the most important and urgent issues in the 21st century. In this regard, semiconductor photocatalysis technology is of great interest, since it can produce clean hydrogen by the direct utilization of solar energy. Since Fujishima and Honda first discovered that, under UV light irradiation, water can be decomposed to produce H_2, using a TiO_2 electrode, numerous studies on TiO_2 have been conducted in detail to explain the reaction mechanism and to improve the photocatalytic efficiency [1,2]. TiO_2 has been considered the most widely investigated photocatalyst for H_2 production because it possesses some significant advantages, such as superior stability, non-toxicity, and low cost [3,4]. However, the more widespread application of TiO_2 in photocatalysis is greatly restricted, due to the low quantum yield and low efficiency of sunlight utilization, mainly resulting from its relatively wide bandgap of about 3.2 eV [5–7]. Thus, it is imminently necessary to probe novel compounds with outstanding photocatalytic properties under visible light irradiation [8,9].

In recent years, bismuth-based semiconductors, as one kind of new photocatalytic material, have been widely studied [10,11]. These compounds usually contain trivalent or pentavalent states of bismuth. It is worth noting that bismuth-based semiconductor photocatalysts possess a unique electronic structure. A continuously uplifted valence band, which reduces the band gap, is formed, due to the hybridization of O-2p and Bi-6s orbitals [12]. Bi^{5+} has a different electronic structure from the trivalent bismuthate, with an

empty 6s orbital, but still has a d10 blocking shell [13]. The light absorption range of these materials is expanded, due to this unique feature, which leads to improved photocatalytic performance. Among the bismuth-based compounds, $MgBi_2O_6$ (MBO), with its trirutile-type structure, can be considered a visible light-responsive photocatalyst, which possesses a relatively small band gap of 1.8 eV [14]. However, compared with other well-studied photocatalysts, the photocatalytic efficiency of MBO is relatively low, which may be due to its low redox ability, mainly resulting from the narrow band gap.

Currently, one of the most valid and executable pathways to obtain a new material with significantly enhanced photocatalytic performance is to construct a semiconductor heterojunction, through combining semiconductors with different band gaps [15–17]. The synthesized heterostructured composites generally possess obviously enhanced photocatalytic activity, since the photoinduced electrons and holes are effectively separated and transferred to the heterojunction under the driving force of the internal electric field, and plenty of holes and electrons participating in redox reactions would be generated [18,19]. Many heterojunctions have been applied to promote photocatalytic reactions, and TiO_2-based heterojunction photocatalysts, in particular, have been widely studied. For instance, Peng and co-authors reported that $AgIn_5S_8/TiO_2$ composites exhibited significantly enhanced photocatalytic performance in the production of H_2 because of the heterojunction structure built between $AgIn_5S_8$ and TiO_2 [20]. Currently, MBO/TiO_2 composites have not been reported, and the improvement in photocatalytic H_2 production of TiO_2, induced by the addition of MBO, needs to be investigated in detail.

In the present paper, we successfully synthesized the MBO/TiO_2 composite photocatalysts using a one-step hydrothermal method. Compared with pure MBO and TiO_2, the photocatalytic performance of the MBO/TiO_2 composites clearly improved and the H_2 production rate under visible light significantly improved. The corresponding photocatalytic reaction mechanism was discussed further.

2. Materials and Methods

2.1. Synthesis of MBO Nanospheres and MBO/TiO_2 Photocatalysts

All synthetic chemicals were analytically pure and required no additional purification. Pure MBO was synthesized using a hydrothermal method. $NaBiO_3 \bullet 5H_2O$ (x = 0.025, 0.1, 0.2, 0.3, and 1.5 mmol) was dissolved in 30 mL of water with about 10 min of strong stirring to obtain solution A. $MgCl_2 \bullet 2H_2O$ (4x mmol) was dispersed in 30 mL of pure water and stirred for about 10 min to obtain solution B. Then, the orange mixed solution was obtained by mixing solution A with solution B and vigorously stirring for 30 min. Under the stirring state, 0.7987 g of TiO_2 (Degussa P25, Frankfurt, Germany) was gradually added to the mixed solution. The pH value of the mixture was kept at 8.5 by adding 4 mol/L of NaOH solution. The mixture was kept at 130 °C for 6 h in a 100 mL stainless steel autoclave. After this, the mixture in the autoclave was filtered to obtain the crude product. The final product was obtained via washing with pure water, as well as with absolute ethanol, several times, and then dried at 60 °C for 12 h. In this article, the molar ratios of MBO to TiO_2 were 0.01%, 0.05%, 0.2%, 0.6% and 3%, which were represented as $0.01MBO/TiO_2$, $0.05MBO/TiO_2$, $0.2MBO/TiO_2$, $0.6MBO/TiO_2$ and $3MBO/TiO_2$, respectively.

2.2. Characterization of Samples

The X-ray diffractometer (XRD) (D8 Advance, Bruker, Billerica, MA, USA) was used to obtain the physical phase and used in the purity analysis of samples. The morphologies and microstructures of MBO, TiO_2 and MBO/TiO_2 were characterized using a field emission scanning electron microscope (FESEM) (FEI Quanta 450 FEG, Hillsboro, OR, USA) and a transmission electron microscope (TEM) (FEI Tecnai G20, ThermoFisher, Waltham, MA, USA). The X-ray photoelectron spectroscopy (XPS) (Thermo ESCALAB 250Xi, ThermoFisher, Waltham, MA, USA) was employed to investigate the elemental compositions and oxidation states of the MBO/TiO_2 composites. The ultraviolet–visible (UV–Vis) spectrometer (Puxi TU-1901, PERSEE, Beijing, China) was used to measure

the UV–Vis diffuse reflectance spectroscopy (UV–Vis DRS) of the as-prepared samples, with barium sulfate as the reference. The photocatalytic analysis system (Labsolar-IIIAG, Perfect-light, Beijing, China) was used to examine the production of H_2.

2.3. Photocatalytic Hydrogen Production Test

A 300 W Xe irradiation lamp was placed on the top of the photocatalytic hydrogen production reactor, which was connected to the Labsolar-III (AG) system. In a general test, 0.1 g of the heterostructured composite catalysts was added to the solution, with methanol serving as the sacrificial agent. The irradiation started to work after the air in the system was thoroughly eliminated. An online gas chromatograph (GC7900, Techcomp, Beijing, China) was used to periodically analyze the hydrogen generated from the photocatalytic reaction. The stability of the photocatalyst was checked throughout the experiment cycle. Following the same steps, it was tested 5 times under visible light. Before the reaction started, the system was evacuated and purified with nitrogen to make sure that there was no H_2 or O_2.

2.4. Photoelectrochemical Studies

The photochemical tests were carried out using an electrochemical system (CHI-660B, Tianjin, China). A three-electrode system, with a Na_2SO_4 electrolyte solution (0.1 M), was used in the measurements, in which the synthesized photocatalyst was firstly uniformly plated on the fluorine-doped SnO_2 conductive (FTO) glass sheet with ethanol ultrasonication, and then the binder was added dropwise, followed by drying the plated FTO glass sheet in an oven. After completion, it was removed and used as the working electrode. The saturated calomel electrode was used as the reference electrode and the platinum wire served as the counter electrode.

3. Results and Discussion

3.1. Phase Structure and Morphological Analysis

The crystallinity and composition of MBO, TiO_2 and the MBO/TiO_2 composites, synthesized at 130 °C with a range of molar ratios of MBO to TiO_2, were measured using XRD, and are shown in Figure 1. The XRD peaks at the 2θ values of 18.2°, 20.5°, 26.1°, 32°, 33.3°,37.2°, 50.8°, 53.7° and 64.6° correspond to the (002), (101), (110), (112), (103), (200), (213), (220) and (303) crystal surfaces of pure MBO, respectively. This matches well with the standard card (JCPDS No.86-2492) of MBO. The characteristic peaks of the rutile and anatase phases of TiO_2 can be found in Figure 1, and are well indexed to the standard XRD patterns (JCPDS No.21-1276 and No.21-12). No other crystal phases were found from the XRD patterns of MBO/TiO_2, indicating that the obtained composite material has high purity. It is obvious that, with the increase in the MBO component, the intensities of the XRD peaks of MBO become stronger and the characteristic diffraction peaks of TiO_2 would gradually become weaker. In addition, when the amount of added MBO is less than 0.6%, there are no diffraction peaks of MBO observed. The XRD patterns of 0.2 MBO/TiO_2 indicate that the structures of TiO_2 and MBO remain stable during the preparation of MBO/TiO_2. The sharp and intense diffraction peaks indicate that the product crystallizes very well. The XRD results clearly demonstrate the formation of MBO/TiO_2 composites with good crystallinity via the hydrothermal method.

The measured morphologies and microstructures of pure MBO, TiO_2 and the prepared 0.2 MBO/TiO_2 composites from SEM are placed in Figure 2. It can be observed from Figure 2a,b that pure MBO consists of irregular hexahedron morphologies, with a length and width of about 80~250 nm. The morphology of pure TiO_2, as shown in Figure 2c, is composed of irregular cubic particles, with a size of about 20–50 nm. For the 0.2 MBO/TiO_2 composite shown in Figure 2d, one can observe that the morphology of MBO is transformed from the original hexahedral particles into irregular cubic particles, and a large number of small TiO_2 nanoparticles are homogeneously distributed around the MBO particles. Figure 2e shows the EDS mapping images of the 0.2 MBO/TiO_2 composite nanomaterials, visualizing the distribution of Ti, O, Mg and Bi. The detailed microstructure of the

0.2 MBO/TiO_2 nanocomposite can be further observed by TEM and high-resolution TEM (HRTEM). Figure 2f shows that MBO is in close contact with TiO_2 particles, with a size of about 30–120 nm. It can be found, from the measured lattice fringes of the composite shown in Figure 2g, that the tested lattice parameters are about 0.3516, 0.2187, and 0.3412 nm, and correspond to the (101) plane of anatase TiO_2, the (111) plane of rutile TiO_2 [21], and the (110) plane of MBO, respectively. The interface between TiO_2 and MBO nanoparticles is clear, and can provide a reaction center for the reaction [22]. For the present study, only two components of MBO and TiO_2 formed in the heterojunction, without other impurities.

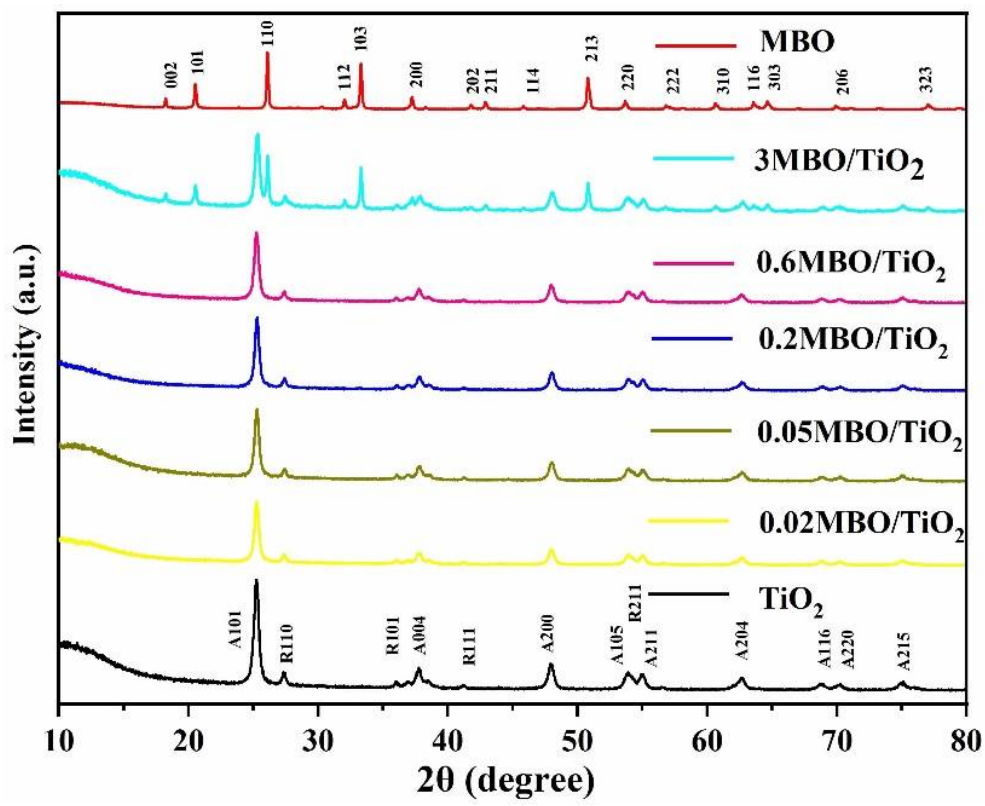

Figure 1. XRD patterns of pure MBO, TiO_2 and the as-prepared MBO/TiO_2 composites with different MBO contents.

To evaluate the elemental status and chemical composition of the prepared samples, the 0.2 MBO/TiO_2 catalyst was further measured using XPS. The full-scan spectrum of 0.2 MBO/TiO_2, as presented in Figure 3a, confirms the existence of Ti, O, Mg, Bi and C elements. Generally, the adventitious hydrocarbons generated from the XPS instrument are considered to be the cause of the occurrence of the C1s peak at about 284.7 eV in the XPS full spectrum. Figure 3b shows that the peak at around 1303.8 eV can be assigned to the Mg1s peak of Mg^{2+} [23]. The peaks at 529.5 eV and 531.2 eV in Figure 3c correspond to the lattice oxygen of the Ti-O/Bi-O bond in O1s, and the chemically adsorbed oxygen [21], respectively. The peaks at around 164.1 eV and 158.5 eV, presented in Figure 3d, correspond to Bi $4f_{5/2}$ and Bi $4f_{7/2}$, confirming the presence of the Bi^{5+} state [14,24]. In Figure 3e, there are two peaks at around 458.8 eV and 464.2 eV, which can be indexed to Ti $2p_{3/2}$ and Ti $2p_{1/2}$, respectively [18], and confirm the presence of Ti^{4+} cations in the MBO/TiO_2 composites [25]. As a result, the measured XPS results have proved the successful synthesis of the MBO/TiO_2 heterostructure.

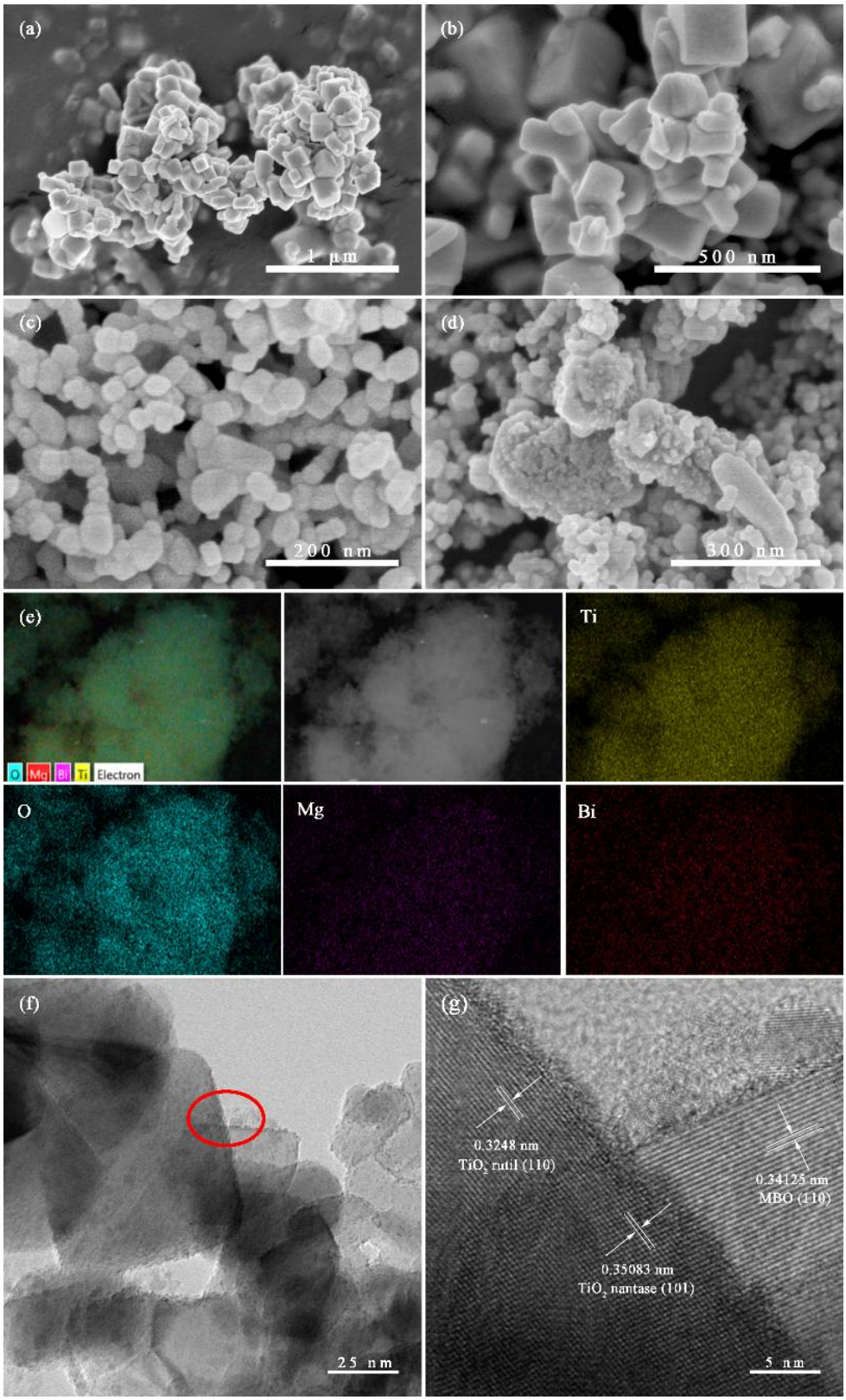

Figure 2. SEM images of (**a**,**b**) MBO, (**c**) TiO_2, (**d**) 0.2 MBO/TiO_2, (**e**) EDS elemental mapping images, (**f**) TEM and (**g**) HRTEM images of 0.2 MBO/TiO_2.

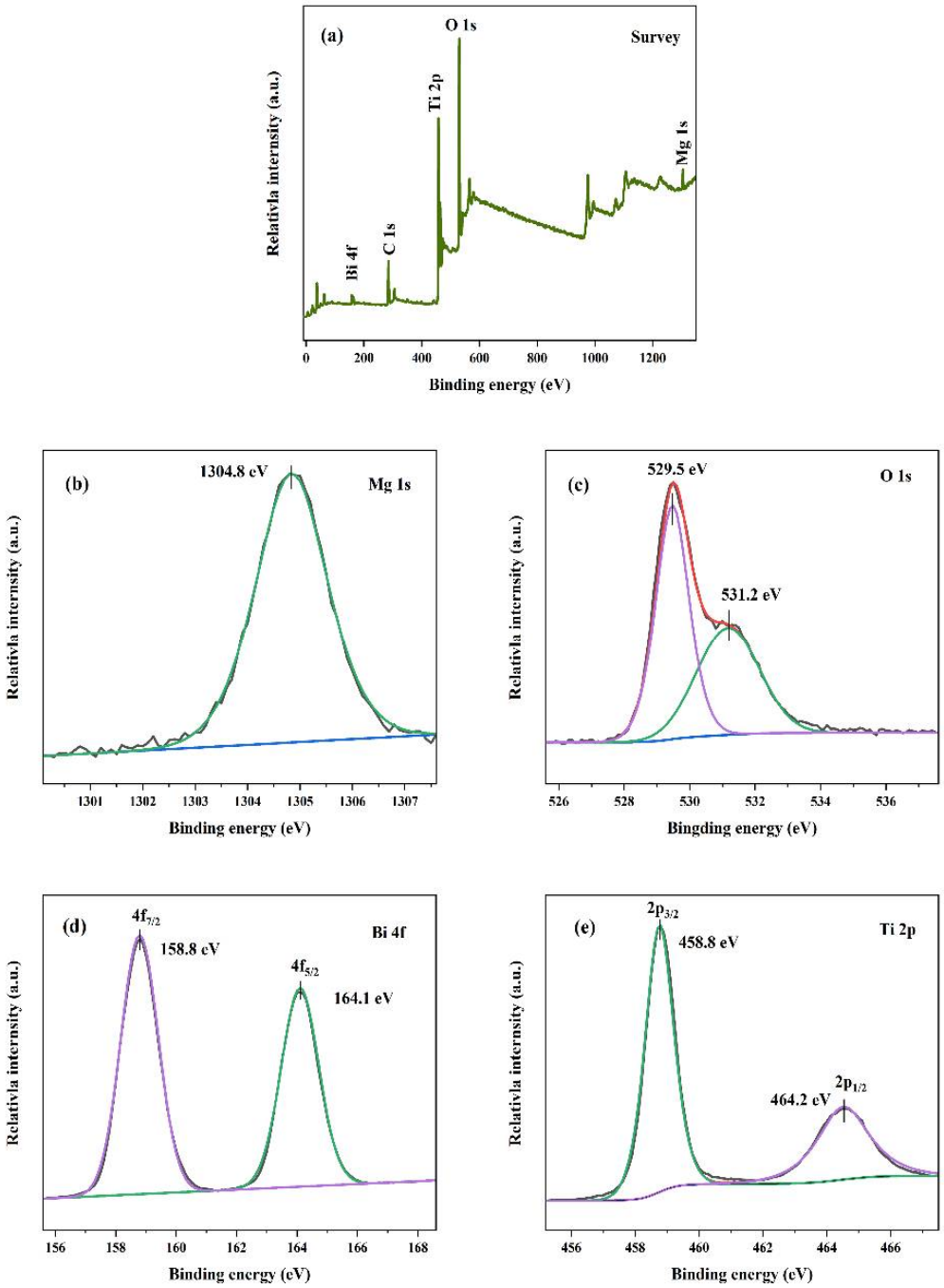

Figure 3. XPS spectra of 0.2 MBO/TiO_2: (**a**) full scan survey of all the elements; (**b**) Mg1s; (**c**) O1s; (**d**) Bi4f; (**e**) Ti2p.

The specific surface area is a factor that affects the catalytic activity of photocatalytic materials, and the specific surface area is generally measured using the N_2 isothermal adsorption and desorption curves. As shown in Figure 4, the N_2 isothermal adsorption and desorption curves of MBO, 0.2 MBO/TiO_2 and TiO_2 were 45.94 cm^2 g^{-1}, 59.69 cm^2 g^{-1} and 30.87 cm^2 g^{-1}, respectively. The measured results show that the prepared 0.2 MBO/TiO_2 composites with larger specific surface areas are expected to possess higher catalytic activity, in comparison with MBO and TiO_2.

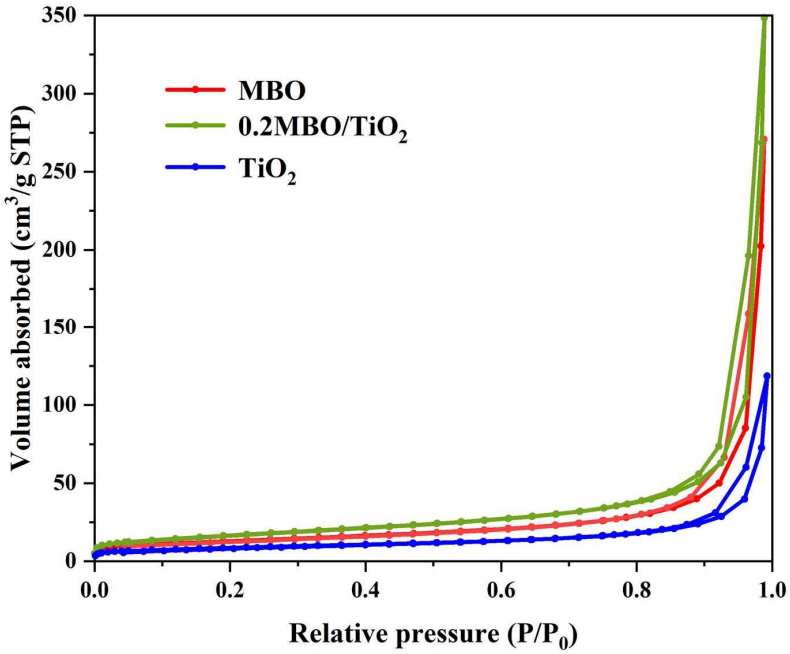

Figure 4. N_2 isothermal adsorption and desorption test curves of MBO, 0.2 MBO/TiO_2 and TiO_2.

3.2. Light Absorption Spectra of MBO/TiO$_2$ Catalysts

The absorption spectra of pure MBO, TiO_2 and the 0.2 MBO/TiO_2 composite photocatalysts were measured using a UV–Vis spectrophotometer, and are presented in Figure 5. We can observe that the absorption edges of pure TiO_2 and MBO are at about 392 nm and 756 nm. A slight redshift of the absorption spectrum of the 0.2 MBO/TiO_2 composite photocatalysts can be found in comparison with pure TiO_2, and its light absorption band edge appears in the visible area greater than 400 nm, which is due to the sensitization of the narrow bandgap structure of MBO [26,27]. The following equation can be used to calculate the energy band gap (E_g) of MBO, TiO_2 and MBO/TiO_2:

$$(F(R)hv)^{1/n} = A(hv - E_g) \quad (1)$$

where $F(R)$, v, h and A represent the diffuse absorption coefficient, optical frequency, Planck's constant and proportionality constant, respectively. The value of n is related to the transition type of the semiconductor (here, $n = 2$ corresponds to the indirect semiconductor in this article). The E_g values of 0.2 MBO/TiO_2, MBO and TiO_2 are 3.1 eV, 1.65 eV and 3.2 eV, respectively. The calculated values for MBO and TiO_2 are similar to the previous reports [14,28]. The E_g of 0.2 MBO/TiO_2 is slightly smaller than that of TiO_2, which indicates that the MBO/TiO_2 composites would have a wider light response range, due to the addition of MBO with a small E_g value.

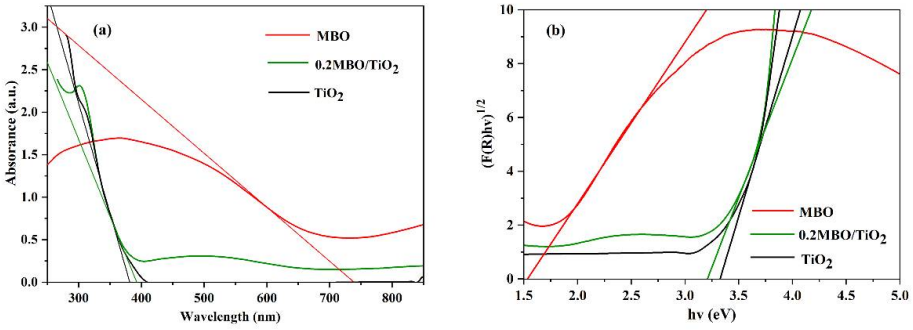

Figure 5. (**a**) UV–Vis DRS and (**b**) the plots of $(F(R)hv)^{1/2}$ versus hv of MBO, TiO_2 and 0.2 MBO/TiO_2.

The measurements of the transient photocurrent response of pure TiO_2, MBO and 0.2 MBO/TiO_2 composite materials, and the corresponding electrochemical impedance spectroscopy (EIS), are helpful for fully understanding the transmission and separation of photogenerated carriers in photocatalysts [22]. Figure 6a clearly shows that the 0.2 MBO/TiO_2 heterostructured composite has a much higher transient photocurrent density compared to pure MBO and TiO_2. This proves that the formation of the MBO/TiO_2 heterojunction accelerates the separation of photogenerated charges and significantly enhances the photocatalytic performance of the composite catalyst. The EIS measurement is then performed to confirm the charge transfer resistance, and the arc radius of the EIS plots can reveal the response rate. The separation of the electron–hole pair and the photocatalytic reaction is faster when the radius of the impedance spectrum arc is smaller. The impedance plot presented in Figure 6b shows that the 0.2 MBO/TiO_2 heterostructured composite has a semicircle with a smaller arc, in comparison with pure MBO and TiO_2, suggesting that the addition of MBO to TiO_2 is beneficial for separating the electron–hole pairs, owing to the reduction in charge transfer resistance; this facilitates the obvious enhancement in the photocatalytic performance of the 0.2 MBO/TiO_2 composite. The normalized plot of the transient photocurrent presented in Figure 6c shows that the transient time constant of the 0.2 MBO/TiO_2 composite is higher than that of MBO and TiO_2, indicating a slower recombination rate [29].

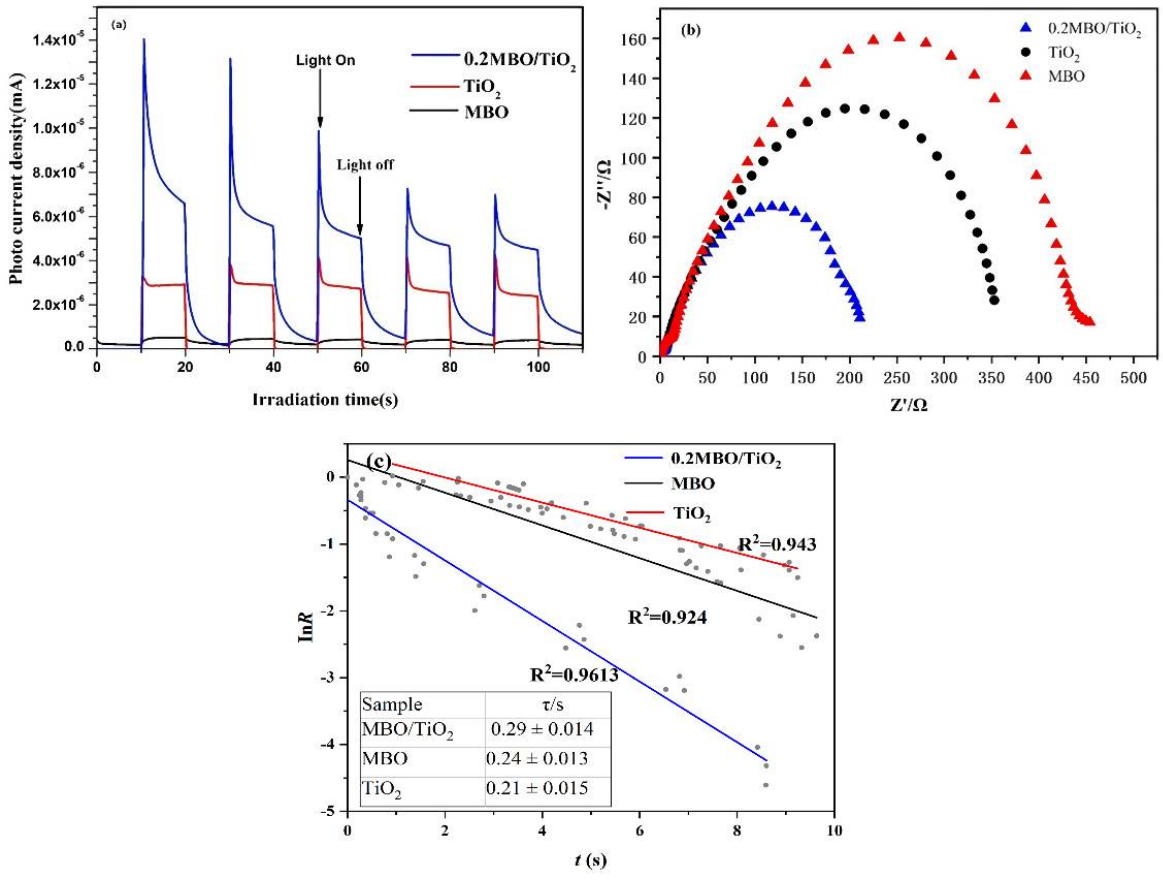

Figure 6. (**a**) Transient photocurrent curves, (**b**) EIS plots, and (**c**) normalized plots of current–time dependence of the MBO, TiO_2 and 0.2 MBO/TiO_2 catalysts, together with the corresponding transient time constants, as shown in the inserted table.

3.3. Hydrogen Production Performance

The measurements of hydrogen production were carried out by adding 0.1 g of catalyst powder to an 80 mL solution, consisting of 20 mL of methanol and 60 mL of deionized water. Figure 7a shows the amount of photocatalytic hydrogen production for

the MBO/TiO_2 composite catalysts under 5 h of visible light irradiation. We can observe that the hydrogen production gradually increases and then decreases with the increase in MBO content. The best loading amount of MBO is about 0.2% and the maximal H_2 production is 15,007 μmol·g^{-1} in 5 h, which is nearly 80 times higher than the hydrogen production of pure TiO_2. Figure 7a also shows that pure MBO is not capable of photocatalytic H_2 evolution. The decrease in H_2 production in the MBO/TiO_2 composites, with a higher MBO content, is probably due to the weakness of catalytic activity on the surface of TiO_2, since the incident light is blocked and the production of electrons by TiO_2 is suppressed because of the high loading amount of MBO [30–33]. The results of the hydrogen production rate of MBO/TiO_2 are shown in Figure 7b. The hydrogen production rate of 0.2 MBO/TiO_2 is 3413 μmol$h^{-1}g^{-1}$, which clearly exceeds that of the samples with other components and single phases. The cycle measurements for MBO/TiO_2 were carried out to confirm the stability of the photocatalyst. The results presented in Figure 7c show that, after the fourth cycle, the H_2 production is 12,275 μmol·g^{-1}, and is about 82% of the first cycle. This indicates the good stability of the 0.2 MBO/TiO_2 photocatalyst. The possible reason for the slight decrease in hydrogen production is that the HCOOH formed by the decomposition of CH_3OH slightly stimulates the activity of the photocatalyst and affects the sensitivity of the photocatalyst to light. Moreover, it can be found from Table 1 that the hydrogen production activity of MBO/TiO_2 is comparable to that of other TiO_2-based heterojunctions, as reported in previous literature.

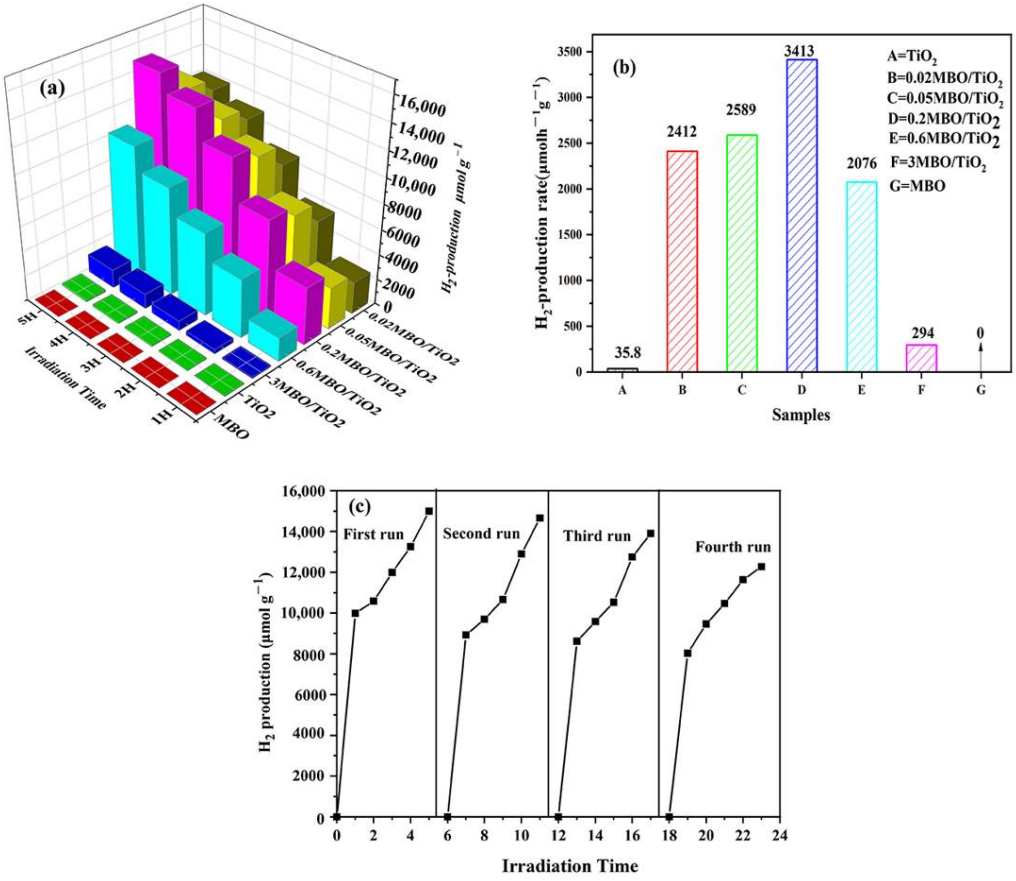

Figure 7. (**a**) Photocatalytic hydrogen generation, (**b**) the hydrogen generation rate of different samples under visible light irradiation, and (**c**) recycling tests for photocatalytic hydrogen generation of 0.2 MBO/TiO_2.

Table 1. A comparison of different TiO_2 composite photocatalysts for hydrogen production.

Photocatalyst	Light Source	Reactant Solution and Sacrificial Reagents	H_2 Evolution Rate	Ref.
$(Sr_{0.6}Bi_{0.305})_2Bi_2O_7/TiO_2$	PLS-SXE 300	Methanol aqueous solution	3.18 mmol h^{-1} g^{-1}	[28]
$AgIn_5S_8/TiO_2$	300 W Xe lamp	Na_2SO_3 and Na_2S aqueous solution	371.1 μmol h^{-1}	[20]
CdS/TiO_2	350 W Xenon lamp	Na_2S aqueous solution	2885 μmol h^{-1} g^{-1}	[34]
SnO_2/TiO_2	Ultraviolet light (UV)	Na_2S and Na_2SO_3 aqueous solution	150 μmol h^{-1} g^{-1}	[35]
$TiO_2/g\text{-}C_3N_4$	300 W Xenon arc lamp	Triethanolamine aqueous solution	39.18 mmol h^{-1} g^{-1}	[36]
$TiO_2/ZnIn_2S_4$	300 W Xenon lamp	Lactic acid aqueous solution	4958 μmol h^{-1} g^{-1}	[37]
MBO/TiO_2	PLS-SXE 300	Methanol aqueous solution	3413 μmol h^{-1} g^{-1}	This work

3.4. Possible Mechanism of Hydrogen Production

Figure 8 shows the Mott–Schottky curves of MBO, 0.2 MBO/TiO_2 and TiO_2 at 2000 Hz. The corresponding flat-band potentials are −1.1 eV, −0.78 eV and −0.85 eV, respectively. All three catalysts have positive slopes on the Mott–Schottky plots, indicating that they all belong to the *n*-type semiconductor. In addition, the flat-band potential of 0.2 MBO/TiO_2 shifts to a less negative value, in comparison with those of MBO and TiO_2 in the single phase. This is also evidence of the formation of an *n*-*n* type heterojunction between MBO and TiO_2.

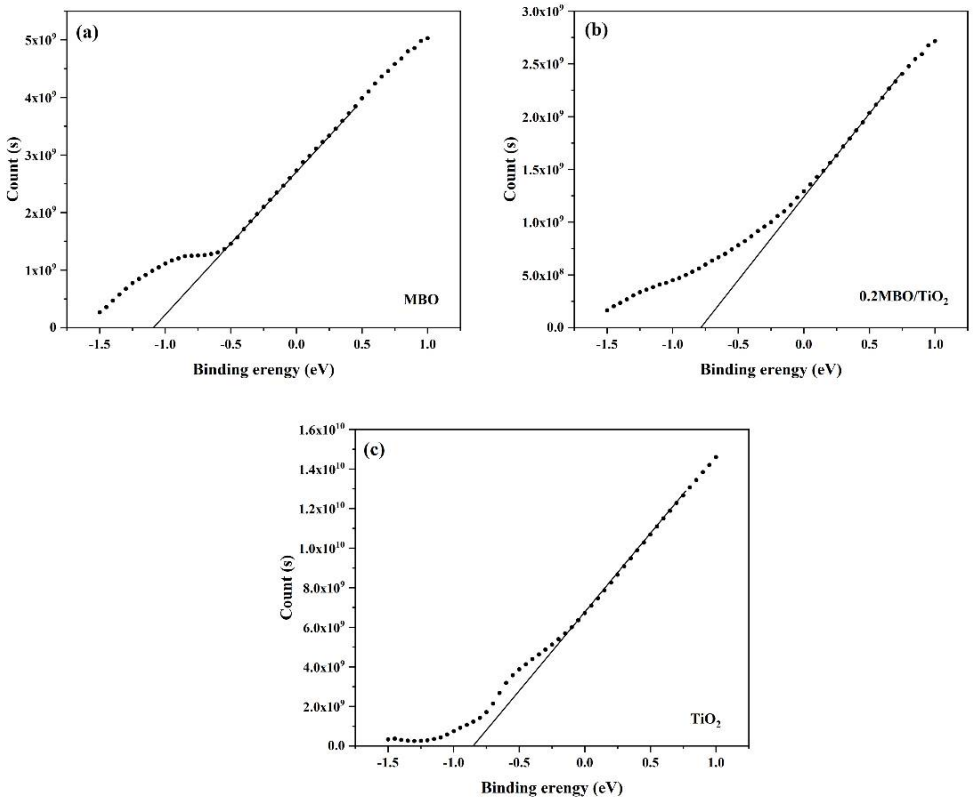

Figure 8. Mott–Schottky plots for (**a**) MBO, (**b**) 0.2 MBO/TiO_2 and (**c**) TiO_2.

The potential mechanism of photocatalytic hydrogen production for MBO/TiO_2 composite catalysts was investigated further, and can be clearly described using a schematic energy band diagram, as shown in Figure 9. First, the edge potential of the conduction band (ECB) and that of the valence band (EVB) for MBO and TiO_2 can be calculated using the following equations [25]:

$$E_{CB} = 0.5E_g + \chi - E_e$$

$$E_{VB} = E_g + E_{CB}$$

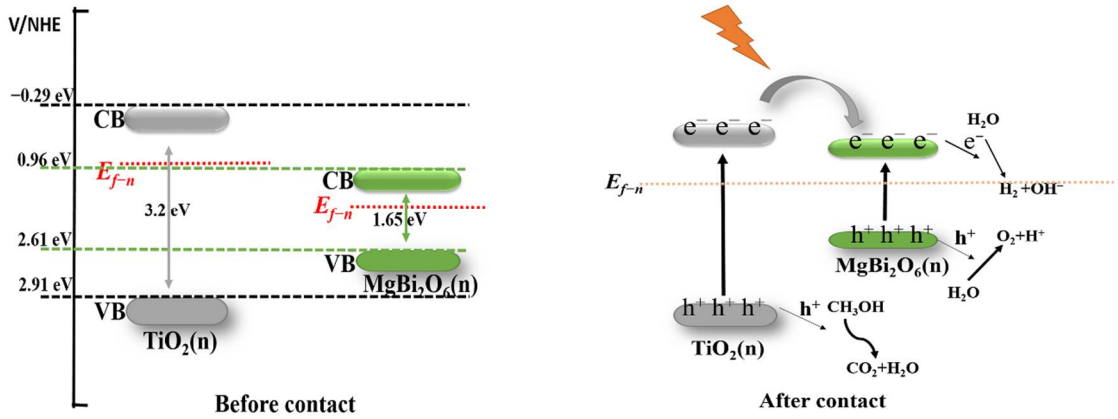

Figure 9. Schematic energy band diagrams of the MBO/TiO_2 *n-n* heterojunction and the possible photocatalytic mechanism of hydrogen production.

Among them, χ is the electronegativity of the semiconductor (6.28 eV for MBO and 5.81 eV for TiO_2). E_e (approximatively 4.5 eV) represents the energy of the free electrons in the standard hydrogen electrode [32]. After calculation, the values of E_{VB} and E_{CB} are 0.96 and 2.61 eV for MBO, and −0.27 and 2.9 eV for TiO_2, respectively.

Based on the above results and considerations, we proposed a possible hydrogen production reaction mechanism for the MBO/TiO_2 composite photocatalytic system. Since the bottom of the conduction band of TiO_2 is higher than MBO, the corresponding top of the valence band is lower than MBO, as shown in Figure 9. On the one hand, when the material is exposed to light, the electrons in the valence band are excited to transfer to the conduction band, and, at the same time, the holes in the valence band are generated [38]. Due to the potential difference between them, the photogenerated electrons are transferred from the conduction band of TiO_2 to the conduction band of MBO, and they react with water to generate H_2 and OH^- on the surface of the catalyst. On the other hand, the holes in the valence band can directly oxidize water to release O_2 and H^+. At the same time, the sacrificial agent methanol will react with OH^- and H^+, under the action of h^+, to produce CO_2 and H_2O, and other non-polluting substances. However, CO_2 is easily soluble in water and is difficult to detect. The heterojunction is an important basis for photocatalysis. We believe that the MBO/TiO_2 composite photocatalytic system can exhibit excellent photocatalytic activity, due to the rapid separation of photogenerated electron–hole pairs, which is accelerated by the MBO/TiO_2 heterojunction.

4. Conclusions

A new MBO/TiO_2 heterojunction composite material, with the highest efficiency for photocatalytic hydrogen evolution, was prepared successfully through a one-step hydrothermal method. The photocatalytic performance of the MBO/TiO_2 composite is clearly superior to that of the single-component material, under visible light. Particularly, it exhibits excellent stability and the highest efficiency of hydrogen production when the molar ratio of MBO to TiO_2 is 0.2%. From the test results and the above-mentioned discussion of the photocatalytic mechanism, it is evident that the separation and transfer of photoinduced electrons and holes are promoted by the formation of the MBO/TiO_2 *n-n* heterojunction, while the electron–hole pairs hardly recombine, which is a key factor in improving the photocatalytic activity.

Author Contributions: Conceptualization, C.H. and H.Z.; methodology, F.X. and D.Z.; validation, Y.Z.; formal analysis, F.X. and D.Z.; investigation, F.X.; resources, F.X.; writing—original draft preparation, F.X. and D.Z.; writing—review and editing, F.X. and C.H.; visualization, F.X. and D.W.; supervision, C.H.; project administration, C.H.; funding acquisition, C.H. and C.T. All authors have read and agreed to the published version of the manuscript.

Funding: This research was funded by the National Natural Science Foundation of China (51761005, 52061006), the Guangxi Natural Science Foundation (2018JJB160017, 2020GXNSFAA159122), the Guangxi Key Laboratory of Information Materials (201010-Z), and the Opening Project of Guangxi Key Laboratory of Calcium Carbonate Resources Comprehensive Utilization (HZXYKFKT201906).

Institutional Review Board Statement: Not applicable.

Informed Consent Statement: Not applicable.

Data Availability Statement: Not applicable.

Conflicts of Interest: The authors declare no conflict of interest.

References

1. Fujishima, A.; Honda, K. Electrochemical photolysis of water at a semiconductor electrode. *Nature* **1972**, *238*, 37–38. [CrossRef] [PubMed]
2. Mills, A.; Davies, R.H.; Worsley, D. Water-purification by semiconductor photocatalysis. *Chem. Soc. Rev.* **1993**, *22*, 417–425. [CrossRef]
3. Fox, M.A.; Dulay, M.T. Heterogeneous photocatalysis. *Chem. Rev.* **1993**, *93*, 341–357. [CrossRef]
4. Hoffmann, M.R.; Martin, S.T.; Choi, W.Y.; Bahnemann, D.W. Environmental applications of semiconductor photocatalysis. *Chem. Rev.* **1995**, *95*, 69–96. [CrossRef]
5. Zou, Z.G.; Ye, J.H.; Sayama, K.; Arakawa, H. Direct splitting of water under visible light irradiation with an oxide semiconductor photocatalyst. *Nature* **2001**, *414*, 625–627. [CrossRef] [PubMed]
6. Kudo, A.; Miseki, Y. Heterogeneous photocatalyst materials for water splitting. *Chem. Soc. Rev.* **2009**, *38*, 253–278. [CrossRef] [PubMed]
7. Chen, C.C.; Ma, W.H.; Zhao, J.C. Semiconductor-mediated photodegradation of pollutants under visible-light irradiation. *Chem. Soc. Rev.* **2010**, *39*, 4206–4219. [CrossRef]
8. Linic, S.; Christopher, P.; Ingram, D.B. Plasmonic-metal nanostructures for efficient conversion of solar to chemical energy. *Nat. Mater.* **2011**, *10*, 911–921. [CrossRef]
9. Meng, X.C.; Li, Z.Z.; Chen, J.; Xie, H.W.; Zhang, Z.S. Enhanced visible light-induced photocatalytic activity of surface-modified BiOBr with Pd nanoparticles. *Appl. Surf. Sci.* **2018**, *433*, 76–87. [CrossRef]
10. Cheng, L.J.; Kang, Y. Synthesis and characterization of Bi_2O_3/$NaBiO_3$ composite visible light-driven photocatalyst. *Mater. Lett.* **2013**, *97*, 125–128. [CrossRef]
11. Shen, J.; Wang, R.; Liu, Q.Q.; Yang, X.F.; Tang, H.; Yang, J. Accelerating photocatalytic hydrogen evolution and pollutant degradation by coupling organic co-catalysts with TiO_2. *Chin. J. Catal.* **2019**, *40*, 380–389. [CrossRef]
12. Kako, T.; Zou, Z.; Katagiri, M.; Ye, J. Decomposition of organic compounds over $NaBiO_3$ under visible light irradiation. *Chem. Mater.* **2007**, *19*, 198–202. [CrossRef]
13. Takei, T.; Haramoto, R.; Dong, Q.; Kumada, N.; Yonesaki, Y.; Kinomura, N.; Mano, T.; Nishimoto, S.; Kameshima, Y.; Miyake, M. Photocatalytic activities of various pentavalent bismuthates under visible light irradiation. *J. Solid State Chem.* **2011**, *184*, 2017–2022. [CrossRef]
14. Zhong, L.S.; Hu, C.H.; Zhuang, J.; Zhong, Y.; Wang, D.H.; Zhou, H.Y. AgBr/$MgBi_2O_6$ heterostructured composites with highly efficient visible-light-driven photocatalytic activity. *J. Phys. Chem. Solids* **2018**, *117*, 94–100. [CrossRef]
15. Zhu, D.; Wang, X.L.; An, H.T.; Zhong, Y.; Wang, D.H.; Tang, C.Y.; Hu, C.H. Facile one-step hydrothermal fabrication of $(Sr_{0.6}Bi_{0.305})_2Bi_2O_7$/$SnO_2$ heterojunction with excellent photocatalytic activity. *Nanomaterials* **2020**, *10*, 321. [CrossRef] [PubMed]
16. Meng, S.; Zhang, J.; Chen, S.; Zhang, S.; Huang, W. Perspective on construction of heterojunction photocatalysts and the complete utilization of photogenerated charge carriers. *Appl. Surf. Sci.* **2019**, *476*, 982–992. [CrossRef]
17. Hu, C.H.; Zhuang, J.; Zhong, L.S.; Zhong, Y.; Wang, D.H.; Zhou, H.Y. Significantly enhanced photocatalytic activity of visible light responsive AgBr/$Bi_2Sn_2O_7$ heterostructured composites. *Appl. Surf. Sci.* **2017**, *426*, 1173–1181. [CrossRef]
18. Nanu, M.; Schoonman, J.; Goossens, A. Solar-energy conversion in TiO_2/$CuInS_2$ nanocomposites. *Adv. Funct. Mater.* **2005**, *15*, 95–100. [CrossRef]
19. Ju, P.; Wang, Y.; Sun, Y.; Zhang, D. Controllable one-pot synthesis of a nest-like Bi_2WO_6/$BiVO_4$ composite with enhanced photocatalytic antifouling performance under visible light irradiation. *Dalton Trans.* **2016**, *45*, 4588–4602. [CrossRef]
20. Li, K.; Xu, J.L.; Zhang, X.H.; Peng, T.Y.; Li, X.G. Low-temperature preparation of $AgIn_5S_8$/TiO_2 heterojunction nanocomposite with efficient visible-light-driven hydrogen production. *Int. J. Hydrog. Energy* **2013**, *38*, 15965–15975. [CrossRef]
21. Khojasteh, F.; Mersagh, M.R.; Hashemipour, H. The influences of Ni, Ag-doped TiO_2 and SnO_2, Ag-doped SnO_2/TiO_2 nanocomposites on recombination reduction in dye synthesized solar cells. *J. Alloy. Compd.* **2022**, *890*, 161709. [CrossRef]
22. Ou, H.H.; Lo, S.L.; Liao, C.H. N-Doped TiO_2 prepared from microwave-assisted titanate nanotubes ($Na_xH_{2-x}Ti_3O_7$): The effect of microwave irradiation during TNT synthesis on the visible light photoactivity of N-Doped TiO_2. *J. Phys. Chem. C* **2011**, *115*, 4000–4007. [CrossRef]
23. Minakshi, M.; Mitchell, D.R.G.; Munnangi, A.R.; Barlow, A.J.; Fichtner, J. New insights into the electrochemistry of magnesium molybdate hierarchical architectures for high performance sodium devices. *Nanoscale* **2018**, *10*, 13277–13288. [CrossRef] [PubMed]

24. Wang, X.L.; Liu, L.; An, H.T.; Zhong, Y.; Wang, D.H.; Tang, C.Y.; Hu, C.H. $(Sr_{0.6}Bi_{0.305})_2Bi_2O_7$ as a new visible-light-responsive photocatalyst: An experimental and theoretical study. *Mater. Res. Bull.* **2019**, *118*, 110484. [CrossRef]
25. Zhang, W.N.; Zhang, Q.G.; Wang, X.H.; Yan, X.X.; Xu, J.Q.; Zeng, Z.G. Lead-free organic-inorganic hybrid perovskite heterojunction composites for photocatalytic applications. *Catal. Sci. Technol.* **2017**, *7*, 2753–2762. [CrossRef]
26. Feizpoor, S.; Habibi-Yangjeh, A.; Vadivel, S. Novel TiO_2/Ag_2CrO_4 nanocomposites: Efficient visible-light-driven photocatalysts with n-n heterojunctions. *J. Photochem. Photobiol. A Chem.* **2017**, *341*, 57–68. [CrossRef]
27. Mizoguchi, H.; Bhuvanesh, N.S.P.; Woodward, P.M. Optical and electrical properties of the wide gap, n-type semiconductors: $ZnBi_2O_6$ and $MgBi_2O_6$. *Chem. Commun.* **2003**, *9*, 1084–1085. [CrossRef]
28. Wang, X.L.; Hu, C.H.; An, H.T.; Zhu, D.; Zhong, Y.; Wang, D.H.; Tang, C.Y.; Sun, L.X.; Zhou, H.Y. Photocatalytic removal of MB and hydrogen evolution in water by $(Sr_{0.6}Bi_{0.305})_2Bi_2O_7/TiO_2$ heterostructures under visible-light irradiation. *Appl. Surf. Sci.* **2021**, *544*, 148920. [CrossRef]
29. Spadavecchia, F.; Ardizzone, S.; Cappelleetti, G.; Falciola, L.; Ceotto, M.; Lotti, D. Investigation and optimization of photocurrent transient measurements on nano-TiO_2. *J. Appl. Electrchem.* **2013**, *43*, 217–225. [CrossRef]
30. Pragathiswaran, C.; Smitha, C.; Abbubakkar, B.M.; Govindhan, P.N.; Krishnan, A. Synthesis and characterization of TiO_2/ZnO–Ag nanocomposite for photocatalytic degradation of dyes and anti-microbial activity. *Mater. Today Proc.* **2021**, *45*, 3357–3364. [CrossRef]
31. Ding, Y.B.; Zhang, G.L.; Wang, X.R.; Zhu, L.H.; Tang, H.Q. Chemical and photocatalytic oxidative degradation of carbamazepine by using metastable Bi^{3+} self-doped $NaBiO_3$ nanosheets as a bifunctional material. *Appl. Catal. B Environ.* **2017**, *202*, 528–538. [CrossRef]
32. Devi, L.G.; Kavitha, R. A review on plasmonic metal-TiO_2 composite for generation, trapping, storing and dynamic vectorial transfer of photogenerated electrons across the Schottky junction in a photocatalytic system. *Appl. Surf. Sci.* **2016**, *360*, 601–622. [CrossRef]
33. Wang, X.; Li, Z.; Zhang, Y.; Li, Q.; Du, H.; Liu, F.; Zhang, X.; Mu, H.; Duan, J. Enhanced photocatalytic antibacterial and degradation performance by p-n-p type $CoFe_2O_4/CoFe_2S_4/MgBi_2O_6$ photocatalyst under visible light irradiation. *Chem. Eng. J.* **2022**, *429*, 132270. [CrossRef]
34. Ren, F.M.; Ma, H.H.; Hu, W.; Zhou, Z.F.; Xu, W.B. Preparation of Sn-doped CdS/TiO_2/ conducting polymer fiber composites for efficient photocatalytic hydrogen production under visible light irradiation. *J. Appl. Polym. Sci.* **2015**, *132*, 42300. [CrossRef]
35. Xu, X.; Yang, G.R.; Liang, J.; Ding, S.J.; Tang, C.L.; Yang, H.H.; Yan, W.; Yang, G.D.; Yu, D.M. Fabrication of one-dimensional heterostructured TiO_2@SnO_2 with enhanced photocatalytic activity. *J. Mater. Chem. A* **2014**, *2*, 116–122. [CrossRef]
36. Chen, W.; Liu, T.Y.; Huang, T.; Liu, X.H.; Duan, G.R.; Yang, X.J.; Chen, S.M. A novel yet simple strategy to fabricate visible light responsive C, N-TiO_2/g-C_3N_4 heterostructures with significantly enhanced photocatalytic hydrogen generation. *RSC Adv.* **2015**, *5*, 101214–101220. [CrossRef]
37. Chen, H.; Li, Z.-H.; Zhao, L.; Yang, G.-D. Synthesis of TiO_2@$ZnIn_2S_4$ hollow nanospheres with enhanced photocatalytic hydrogen evolution. *Rare Met.* **2019**, *38*, 420–427.
38. Low, J.; Yu, J.; Jaroniec, M.; Wageh, S.; Al-Ghamdi, A.A. Heterojunction photocatalysts. *Adv. Mater.* **2017**, *29*, 1601694. [CrossRef]